Preprints are preliminary reports that have not undergone peer review.
They should not be considered conclusive, used to inform clinical practice,
or referenced by the media as validated information.

# Wafer-scale Fabrication of CMOS-compatible Trapping-mode Infrared Imagers with Colloidal Quantum Dots

**Xin TANG** ( xintang@bit.edu.cn )
Beijing Institute of Technology https://orcid.org/0000-0003-0008-207X
**Shuo Zhang**
Beijing Institute of Technology
**Cheng Bi**
Zhongxinrecheng Science and Technology co.,ltd
**Tianling Qin**
Beijing institute of technology
**Yanfei Liu**
Zhongxinrecheng Science and Technology co.,ltd
**Jie Cao**
Beijing Institute of Technology
**Jiaqi Song**
Beijing Institute of Technology
**Yongjun Huo**
Beijing Institute of Technology
**Menglu Chen**
Beijing Institute of Technology
**Qun Hao**
Beijing Institute of Technology

---

**Article**

**Keywords:** Infrared, Colloidal Quantum Dots, Imager, CMOS-compatible

**Posted Date:** October 20th, 2022

**DOI:** https://doi.org/10.21203/rs.3.rs-2076887/v1

**License:** This work is licensed under a Creative Commons Attribution 4.0 International License.
Read Full License

---

# Abstract

Silicon-based complementary metal-oxide-semiconductors (CMOS) devices have dominated the technological revolution in the past decades. With increasing demands in machine vision, autonomous driving, and artificial intelligence, Si-CMOS imagers, as the major optical information input devices, face great challenges in spectral sensing ranges. In this paper, we demonstrate the development of CMOS-compatible infrared colloidal quantum dots (CQDs) imagers in the broadband short-wave and mid-wave infrared ranges (SWIR and MWIR, 1.5-5μm). A new device architecture of trapping-mode detector is proposed, fabricated, and demonstrated with lowered dark currents and improved responsivity. The CMOS-compatible fabrication process is completed with two-step sequential spin-coating processes of intrinsic and doped HgTe CQDs on an 8-inch CMOS readout wafer with photoresponse non-uniformity (PRNU) down to 4%, dead pixel rate of 0%, external quantum efficiency up to 175%, and detectivity as high as $2\times10^{11}$Jones for extended SWIR (cut-off wavelength=2.5μm) @ 300K and $8\times10^{10}$Jones for MWIR (cut-off wavelength=5.5μm) @ 80K. Both SWIR images and MWIR thermal images are demonstrated with great potential for semiconductor inspection, chemical identification, and temperature monitoring.


# Introduction

Optoelectronics based on complementary metal-oxide-semiconductors (CMOS) plays vital roles in the technological revolution over the past decades. Benefitted from the CMOS technology, silicon-based imagers have been developed with superior resolution, large format, and on-chip processing functionalities (deep learning [1,2], optoelectronic computing [3–5], neuromorphic computing [6] ) and are implemented in almost every consumer electronics system including cell phones, automobiles, and surveillance systems. The key to the huge success of silicon imagers includes their CMOS compatibility which enables high uniformity across a large area, low cost, and scalable fabrication. However, due to the limitation of silicon's energy bandgap (~1.1eV), the spectral sensing ranges of current CMOS imagers are confined within visible (0.4-0.7 μm) and near-infrared regions (0.8-1.1 μm), while vast demands and opportunities reside in the rest of the wide spectral regions.

Going beyond visible, infrared, especially short-wave infrared (1.5-2.5 μm) and mid-wave infrared (3-5 μm) can be used in gas sensing [7], autonomous driving [8], and remote sensing [9], due to its unique capabilities like identification of chemical's molecular vibrations, deep penetration depth in haze conditions, and high sensitivity to "night glow" radiation. Unfortunately, the dominant infrared materials are binary and ternary bulk semiconductors like InGaAs, InSb, and HgCdTe, which require lattice-matched substrates for growth and complicated flip-bonding process to connect with silicon integrated readout circuits (ROICs) (**Figure. 1a**). Only a single die can be processed at one time, leading to high cost and low production yield, and the processing complexity and cost would increase dramatically with a larger array and smaller pixel size [10]. To further extend the array-format and sensing ranges of Si-CMOS imagers, copper-copper bonding techniques and germanium silicon (GeSi) SWIR imagers have been proposed and

investigated [11]. The difficulty in integrating non-silicon materials with silicon integrated circuits greatly hinders the development of CMOS-compatible imagers beyond visible.

For an array-format imager, array and pixel size, photo-response non-uniformity (PRNU), dead pixel rate, and darkcurrent density are all important figures of merit. Two technological challenges need to be solved before the implementation of high-performance CMOS-compatible infrared imagers. The first challenge lies in the fabrication compatibility of sensing materials with complex surface conditions on ROICs including both oxides and metals. The second challenge is the choice of a suitable device configuration that enables high injection efficiency, high quantum efficiency, low darkcurrent (avoid saturation and blooming [12]), and fast response.

With extensive efforts over years, CMOS-compatible integration or monolithic integration of non-silicon sensing materials with Si-ROICs have been solved by the solution processability of various emerging materials like inorganic-organic metal halide perovskites [13–15], organic polymers [16], and colloidal quantum dots (CQDs) [17–19]. Perovskite X-ray imagers[13] with sensitivity up to 9300 μC $Gy^{-1}cm^{-2}$ and organic polymer ultraviolet-visible detector array[16] with an external quantum efficiency of 40% have already been demonstrated. However, in the infrared region, despite several imagers having been developed and demonstrating imaging capabilities, there remain technological obstacles to improving imaging quality. An initial attempt was made in the near-infrared regions with lead sulfide (PbS) CQDs-sensitized organic photodiodes on a 256×256 thin film transistor (TFT) backplane [20]. The TFT imagers operated at photovoltaic mode with vertically stacked electron/hole transport layers and sensing materials. To compensate for the loss of illuminated optical power through a metal top contact, a high bias voltage of -5V was employed with a large darkcurrent density of ≥1μA/$cm^2$. Besides, external multiplexers and amplification circuits were needed to drive, select, and read the pixel currents. To miniaturize the infrared imager, graphene-PbS CQDs phototransistors with maximum response wavelength at 1.85 μm were transferred onto Si-ROICs that incorporate pixel-level amplification and multiplexing ability [21]. The phototransistor imagers were fabricated by transferring graphene films as conductive channels. A thin layer of PbS CQDs was spun-coated as a light absorber. Due to the limited size of the transferred graphene, the reported graphene-CQDs imagers showed a high dead pixel rate (~15%) with a low filling factor, a slow response time (~10 ms ), and inevitably large darkcurrent due to the high conductance of graphene channels. By using PbS CQDs photodiodes as sensing element, the darkcurent can be greatly reduced and demonstrated high-performance imaging in the near-infrared range (0.7-1.4μm) [22].

To further extend the spectral response ranges, mercury telluride (HgTe) CQDs photoconductors have been used to construct infrared imagers with array size of 320 × 256 [17,18]. With the usage of HgTe CQDs, the spectral response ranges were extended into MWIR. However, the small energy gaps in MWIR, the difficulty in precise control of doping and the photoconductive configuration together led to large darkcurrent (440 μA/$cm^2$), and low external quantum efficiency below 2%. It is true that the solution-processability allows straightforward CMOS-integration, and photodiodes, photoconductors and

phototransistors have all been investigated for infrared CMOS-imagers. However, such integration does not guarantee high performance infrared imaging, highlighting the urgent and challenging needs to develop CMOS-compatible infrared device configuration to enable wide spectral response, high sensitivity, and low power-consumption.

In this paper, we report a new CMOS-compatible infrared device architecture named trapping-mode photodetectors, in which the minority carriers were trapped by a vertical built-in potential leading to both decreased darkcurrent density and improved quantum efficiency. The CMOS-compatible trapping-mode infrared imager was fabricated with HgTe CQDs, as HgTe CQDs have demonstrated so far the highest spectral tunability in mid-infrared regions. Both SWIR and MWIR imagers were demonstrated with unprecedented image quality. The fabrication process is straightforward with two-step sequential spin-coating processes of intrinsic and doped CQDs on an 8-inch ROICs wafer. In one batch, over 200 HgTe CQDs imager chips can be fabricated (**Figure. 1b**). The HgTe CQDs trapping-mode CMOS-imagers showed excellent photoresponse non-uniformity (PRNU) down to 4%, dead pixel rate of 0%, external quantum efficiency up to 175%, and detectivity as high as $2\times10^{11}$Jones for SWIR (cut-off wavelength=2.5μm) @ 300K and $8\times10^{10}$Jones for MWIR (cut-off wavelength=5.5μm) @ 80K.

# Trapping-mode Photodetectors

The device architecture of the trapping-mode photodetector is shown in **Figure. 2a**. It is similar to a photoconductor, except that an n-doped (or p- doped) CQDs layer is added on top of the intrinsic CQDs channel as an electron (or hole) trapping layer. Considering the much denser hole states of HgTe CQDs, we assume the majority of photocarriers for HgTe CQDs are holes [23], and we added n-type CQDs with a doping level of $0.9 \pm 0.08$ |e|/dot on top of the intrinsic CQDs layers, which create a vertical built-in potential that separates photo-excited carriers, drives and traps electrons near the n-type layer. As indicated by the energy band diagram, the photogenerated carriers would go through three stages: generation, separation, and trapping & transportation (**Figures. 2a and b**).

Our HgTe CQDs photodetectors work as photon detectors. The detection starts with the absorption of an incident photon with energy higher than the CQDs' energy gaps. After absorption, a pair of electron and hole will be generated, which is the photocarrier generation process. The excited photocarriers go through two possible processes, separation or recombination. The typical recombination time for HgTe CQDs is 1ns [24]. Therefore, without an external or internal electric field, the photocarrier will recombine and vanish. To generate photocurrents, an external bias voltage is applied in the photoconductive detector; the built-in potential is induced in photovoltaic detectors. Trapping-mode photodetectors combine the external electric and internal electric fields together. Trapping-mode photodetectors share a similar configuration with photoconductors, which has a pair of electrodes to generate a lateral electric field to separate and drive the activated holes and electrons. The uniqueness of trapping-mode photodetectors is the presence of a vertical built-in potential that drives the minority carriers (electrons) towards the top layer of HgTe CQDs film. Therefore, the excited electrons will be trapped there, leaving the majority carrier (holes) in the conductive channel and elongating its lifetime. Eventually, the trapped electrons in the top layer of HgTe

CQDs will recombine near the electrodes. Before recombination, the majority carriers (holes) will be circulating multiple times in the conductive channels, leading to photoconductive gains. The photoconductive gain g can be calculated by

$$g = \frac{t_{lifetime}}{t_{tr}} = \frac{t_{lifetime}}{L/v_{drift}} = \frac{t_{lifetime} \cdot V_{bias} \cdot \mu}{L^2}$$

1

where $t_{tr}$ is transit time, and $t_{lifetime}$ is the carrier lifetime of the majority carrier. The transit time $t_{tr}$ can be estimated by the length of conductive channel $L$ and drift velocity $v_{drift} = E \bullet \mu = (V_{bias} \bullet \mu)/L$, where $V_{bias}$ is the applied bias voltage and $\mu$ is the carrier mobility. To verify the photoconductive gain effect, the response time of a HgTe CQDs photoconductor before and after the addition of the top n-type layer was measured. The results show that the response time increases from 0.8 μs to 17μs (**Figure. S1**). We attribute the increase in response time to the trapping process of electrons. The corresponding photoconductive gain $g$ is ~ 21. Fortunately, the integration time of the focal plane imager is typically on the order of microseconds. Therefore, the trapping-mode HgTe CQDs imager can still output real-time video without image lags.

The concept of a trapping-mode photodetector is similar to a phototransistor. PbS CQDs-graphene [25,26] and HgTe CQDs-$MoS_2$[27] have all been reported. The advantage of using graphene or $MoS_2$ as a conductive channel is that they have high mobility. Therefore, the photoconductive gain, defined as the ratio of the minority carriers' lifetime over the majority carriers' transit time, can be high. High-performance phototransistors have been reported with high responsivity up to $10^7$A/W [25]. However, two-dimensional materials also have much higher conductivity than CQDs film, leading to high darkcurrents. For single-element detectors, the large darkcurrent can be offset with sophisticated external amplification and subtraction circuits. However, in ROICs, the integration capacitor has limited full-well capacity. Large darkcurrents could saturate the integration capacitor. More importantly, the solution-processability of CQDs enables easy integration with ROICs. Two dimensional materials can be transferred onto the ROICs by using sacrificial layers, but it is challenging to obtain full coverage and good electrical connection over large area [21].

To precisely control the doping of HgTe CQDs, a mixed-phase ligand exchange method was developed, which involved liquid phase ligand exchange, doping modification by additional salts, and solid-phase ligand exchange. In liquid phase ligand exchange, β- mercaptoethanol (β-ME) was added to replace the original oleyamine (OAM) ligands on HgTe CQDs. At the same time, CQDs would be transferred from a non-polar solution of hexane to a polar solution like N, N-Dimethylformamide(DMF) and stabilized (**the inset of** Fig. 2c). Then, $HgCl_2$ or $(NH_4)_2S$ salt would be added to CQDs/DMF mixture to introduce additional surface dipoles [28,29]. $Hg^{2+}$ would stabilize electrons in CQDs by surface dipoles, resulting in more n-type CQDs, while the $S^{2-}$ would do the opposite. The CQDs are precipitated and redispersed in DMF to remove extra ligands. Then, CQDs solids are prepared by spin-coating, followed by solid-phase

ligand exchange with 1,2-Ethanedithiol (EDT) and HCl. EDT has two thiols and provides a stronger attachment to HgTe CQDs, and HCl treatment would stabilize the Fermi level in the CQDs solids. As demonstrated by the field-effect transistor measurements, the doping level can be widely tuned from 0.9|e|/dot (n-type), 0.002 |e|/dot (intrinsic), to 0.8 |e|/dot (p-type) (**Figure. 2c**). More importantly, benefitted from the absence of a long-chain thiol group, the carrier mobility was improved to 1–2 $cm^2V^{-1}s^{-1}$ over wide operation temperature from 300 to 80K (**Supplementary Section. S2 and Figure. S2**).

For typical trapping-mode photodetectors, the thickness of the intrinsic and doped layers are 350 nm and 50 nm, respectively (**Figure. 2d**). As a representative detector, SWIR HgTe CQDs trapping-mode detectors with a cutoff wavelength of 2.5μm were fabricated and characterized. The first striking feature of the trapping-mode photodetector is the reduced darkcurrent density from 1.15 $\mu A/mm^2$ to 5.57 $nA/mm^2$ under a bias voltage of 2V at room temperature (Figure. 2e), which is in a similar order to the previously reported darkcurrent density of photovoltaic CQDs imagers (33nA/mm2 under bias voltage of ~ 0.2 V@ 25°C [30], 2.5nA/mm2 ~ 2 V@ 60°C [31] ). Compared with the reference detectors without the n-doped trapping layer, two to three orders of magnitude decreases were observed, and we attribute this to the induced built-in potential inside the trapping-mode photodetectors. Since the doping can be well controlled, the residual carrier density in the intrinsic layer can be as low as 0.002 |e|/dot. Therefore, a substantial depletion width (165–230 nm) can be introduced into the trapping-mode detectors, which minimizes the tunneling leakage current across the vertical junction and leads to lowered darkcurrent (**Supplementary Section. S3**). More importantly, the trap of the minority carriers decreased the recombination rate and elongated the lifetime of the majority carrier, resulting in higher responsivity under the same bias power (Fig. 2f). High responsivity and low bias power are crucial requirements for reduced bias heat load in the large multielement pixels array. Overall, the detectivity of the SWIR photodetectors in trapping mode was improved by at least one order of magnitude (Fig. 2g). In our experiments, trapping-mode photodetectors with HgTe CQDs with various energy gaps have been investigated from 0.5eV to 0.2eV, covering broadband infrared regions with cut-off wavelengths from 2.5 to 5.0 μm (**Figure. 1d**). As shown in Fig. 2h, the trapping-mode photodetectors work for both SWIR and MWIR CQDs.

# Trapping-mode Cmos-imagers

The design of trapping-mode photodetectors is fully compatible with Si-ROICs. A pixel consists of a center pixel electrode and a surrounding guarding ring as common ground (**Supplementary Section. S4 and Figure. S3**). The integration of CQDs with the ROICs can be completed with sequential spin-coating processes. Unlike vertical photodiode structures, no additional contact deposition is needed which greatly reduces the fabrication complexity of CMOS imagers. For optimal detection performance, customized ROICs were designed to match the impedance of our CQDs trapping-mode photodetectors and the deposition of CQDs layers can be conducted with 8-inch wafers (**Figure. 3a**). The ROICs consist of 320×256 pixels with a separation of 30μm. The layout, operation process, defination of I/O pins of the ROICs can be found in **Figure. S4-S5**, and **Table. S1-S2**. **Figure. 3b** showed the packaged HgTe CQDs

CMOS-imager with silicon window to eliminate the influence of visible light. The inset of Fig. 3b shows the ROICs with CQDs films and zoomed view of CQDs pixels.

For an array-format imager, uniform response across the sensing area is the prerequisite for imaging operation. Photoconductor configuration was first employed and characterized as a reference, as shown in **Figure. 3b**. The sensitivity and contrast are low, which is consistent with prior reports about photoconductive imagers[17,18]. Dramatic improvements have been done after the addition of an electron trapping layer of HgTe CQDs on top of the intrinsic photoconductors and clear images with details of a soldering iron were captured. Compared with photoconductors, the addition of top n-type layer induces a vertical built-in potential inside the HgTe CQDs film, which leads to the separation and trapping of minority carriers (electrons). As the lifetime of majority carrier increases, the trapping-mode photodetectors demonstrate photoconductive gains, which improve the photocurrent and quantum efficiency.

A quantitative analysis of the imager was then conducted, as shown in **Figure. 3c**. A calibrated blackbody was used as the excitation light source. Photoresponse from a photoconductor imager was around 0.38 V. In the silicon readout integrated circuits, an integration capacitor is connected to each pixel. When photocurrents are generated. The capacitor will be charged with carriers. The number of charged carriers depends on the magnitude of both photocurrents and integration time. Full well capacity defines the maximum amount of charge an individual pixel can hold before saturating. In our study, the full-well capacity is ~ 15Me-, which corresponds to the maximum output voltage of 3.0V. The amplification factor is ~ 200nV/e-. Therefore, for our array-format HgTe CQDs imagers, the photoresponse is measured by voltage, not ampere.

Based on the incident photon flux from the blackbody and generated electrons, the external quantum efficiency (*EQE*) can be calculated by

$$EQE = \frac{FWC \cdot V_{\mathrm{ph}}/V_{full}}{\phi_{BB} \cdot \Omega \cdot A_{pixel} \cdot t_{\mathrm{int}\,egral}}$$

2

where *FWC* is the full well capacity of 15 Me-, $V_{ph}$ is the photoresponse in volt, $V_{full}$ is the maximum output voltage, $\phi_{BB}$is the photon flux from the blackbody, $\Omega$is the solid angle of the incident photon flux, $A_{pixel}$ is the effective size of a pixel (750 μm$^2$, as shown in **Figure. S3**), and $t_{integral}$ is the integration time for each pixel. For the photoconductor imager, the integration time is 1ms and the calculated *EQE* is around 6.9%, which is in the same order as prior reports about photoconductive MWIR imagers. The photoresponse was fitted by Gaussian distribution, based on which the PRNU was calculated to be 26%. Compared with photoconductors, the PRNU of an electron-trapping photodetector is remarkably low at 4% with a dead pixel rate of 0%. For the electron trapping-mode imager, the photoresponse was improved to 2.4V with an integration time of 0.25ms and the corresponding *EQE* is dramatically increased to 175%.

Considering the thickness of CQDs films, the light absorption should be around 30%. Those results further confirmed the presence of internal gain in trapping-mode photodetectors. With the presence of photoconductive gain of 21, the actual *EQE* could be estimated to be ~ 8.3%, which which is similar to the photoconductive HgTe CQDs imagers without gain mechanism [32]. It is worth noting that hole trapping-mode imagers were also tested with an integration time of 1ms and showed an average *EQE* of 199 % and PRNU of 20%, which is lower than the electron trapping-mode imagers. This is consistent with the fact that for HgTe CQDs, the holes are the major carriers, and the trap of electrons should give optimal performance. The spectral *EQE* can be found in **Figure. S6**.

The noise of the electron trapping-mode photodetectors was also analyzed as shown in **Figure. 3e**. Benefitted from the lowered darkcurrent, the root means square (RMS) noise is 3.5 mV under a bias voltage of 2V. The detectivity of the SWIR imager was then calculated by

$$D^* = \frac{\sqrt{A_{\text{pixel}}}}{V_{rms} \cdot \sqrt{2t_{\text{int}\,egral}}} \cdot \Re = \frac{\sqrt{A_{\text{pixel}}}}{V_{rms} \cdot \sqrt{2t_{\text{int}\,egral}}} \cdot \frac{V_{ph}}{P_{in}}$$

3

At room temperature, our SWIR imagers with cut-off wavelength at 2.5 μm showed excellent detectivity of $2\times10^{11}$Jones with bias voltage below 4 V (**Figure. 3f-h**). Above 4V, the electrical noise from the ROICs increases a lot and can degrade the detectivity with a lower value and broader distribution (**Figure. 3i**). Details of the experimental setup and calculation of parameters for the infrared focal plane array imager can be found in the **supplementary section. S4**. This performance exceeds previously reported HgTe photodiodes at similar wavelengths [27,33–35]. Details of device performance comparison can be found in **Table. S3**. More importantly, the trapping-mode HgTe CQDs imagers break through the current spectral limitation of the InGaAs imager and can be easily extended from 1.7 to 2.5μm with high *EQE* up to 175% and detectivity above $10^{11}$Jones. For MWIR imagers, the detectivity was measured at 80K and the measured detectivity is around $8\times10^{10}$ Jones.

# Swir And Mwir Camera

SWIR and MWIR imagers were fabricated and used to capture infrared images. For SWIR imaging, external lighting from a tungsten lamp or sunlight was required, while the MWIR imager can capture the thermal emissions from room-temperature objects. All SWIR images were captured at room temperature and MWIR imaging was done at 80 K with liquid nitrogen cooling. Prior SWIR infrared imaging mainly captures SWIR photons with a wavelength shorter than 1.8μm. Our HgTe imagers extend the sensing range to 2.5μm, which allows the detection of more infrared information like chemical composition and can be used to develop spectrometers [36]. As shown in **Figure. 4a**, three bottles of water, tetrachloroethylene, and isopropanol behind a silicon wafer were imaged. The opaque silicon becomes almost transparent in the SWIR ranges. The three chemicals showed distinct levels of greyscale due to

the different light absorption strengths of C-H, O-H, and C-Cl bonds. Besides chemical analysis, the SWIR image can distinguish between haze and cloud due to their difference in reflectance, scattering, and absorption (**Figure. 4b**). Transparent polymer glasses and black hair in visible become opaque and white due to the light absorption and reflectance in SWIR ranges (**Figure. 4c**). Figure 4d shows the captured ISO-12233 test chart, based on which the spatial resolution was estimated to be ~ 10lp/mm.

We further demonstrate MWIR imaging results. The MWIR imager was fabricated with HgTe CQDs with a cut-off wavelength of 5.5μm. Unlike SWIR, the MWIR imager detector can sense the emitted infrared radiance from objects and give the temperature distribution of the scene. Figure 4h shows the temperature difference between a cup of cold and hot water. As shown in **Figures. 4e-g** human face, hand, and hot/cold water were captured with detailed temperature information. **Figures. 4h and 4i** show the SWIR and thermal images of the same plastic plant. The results demonstrate the difference in infrared imaging at different wavelengths. The SWIR image can give details of the scene by capturing the specularly reflected light, while thermal images may lose details of objects if the temperature difference between backgrounds is small.

To the best of our knowledge, our HgTe CQDs imagers demonstrated, so far, the widest spectral sensing ranges with high imaging quality, compared with prior infrared CQDs imagers [17,20,21]. It is worth noting that the resolution and pixel size of the HgTe CQDs imagers are defined by the ROICs. Therefore, extending image format and shrinking pixel size should be easily realized with new ROICs. The solution processability of CQDs proves to be essential in low-cost device hybridization. Besides imaging capability, the lifetime and reliability of the CQDs imager were also analyzed by accelerated lifetime measurements. Hallberg Peck model was used in our test with increased humidity and temperature as environment stress [37]. The acceleration factor (*AF*) can be calculated by

$$AF = \left(\frac{RH_t}{RH_u}\right)^n \exp\left[\left(\frac{E_a}{K_B}\right)\left(\frac{1}{Tu} - \frac{1}{Tt}\right)\right]$$

4

where $RH_t$ is the relative humidity in the test chamber, $RH_u$ is the relative humidity in normal working conditions, $n$ is the humidity acceleration constant, which is usually set to be 3, $E_a$ is the activation energy, $K_B$ is the Boltzmann constant, $T_u$ is the temperature in normal working condition and $T_t$ is the relative humidity in the test chamber. For our trapping-mode detector, the major failure mechanism would be the drift or diffusion of surface dopants, which leads to the loss of built-in potential. Therefore, the activation energy $E_a$ is set to be 0.6eV [38]. The CQDs imagers would work at 300K and 25%RH. A programable climatic chamber with a temperature of 365K and 85%RH was used. The *AF* is calculated to be 606. The detectivity is monitored as the major parameter to determine if the imager reaches operation failure. After ~ 200 hours, the detectivity dropped by a factor of 10 and we assume the degradation of performance reaches operation failure. The corresponding lifetime is ~ 14 years (**supplementary section. S6**).

## Conclusions

In conclusion, we developed trapping-mode CMOS-compatible HgTe CQDs imagers. The proposed device architecture is fully compatible with Si-ROICs technology, and we demonstrated both SWIR and MWIR imagers with high-resolution infrared imaging capabilities. The HgTe CQDs trapping-mode CMOS-imagers showed excellent photoresponse non-uniformity (PRNU) down to 4%, dead pixel rate of 0%, external quantum efficiency up to 175%, and detectivity as high as $2\times10^{11}$Jones for SWIR (cut-off wavelength = 2.5μm) @300K and $8\times10^{10}$Jones for MWIR (cut-off wavelength = 5.5μm) @ 80K. With wafer-scale integration, CQDs-based CMOS imagers could lead to cheap infrared sensors that open up numerous potential opportunities in civilian applications like semiconductor inspection, autonomous driving, and spectrometers. Besides easy integration, in the future, the CQDs imagers would also open up the possibility for in-pixel and on-chip fabrication of functional optical structure, as CQDs films can be imprinted with quasi-3D nanostructures [39]. Imagers with functionalities beyond intensity-based imaging may be developed with sensitivity for polarization, phase, and wavelength.

## Methods

# Preparation of n-type, intrinsic, and p-type HgTe CQDs

The mixed-phase ligand exchange process involves 3 steps, including liquid phase ligand exchange, doping modification by additional salts, and solid-phase ligand exchange. In the liquid phase ligand exchange, 10ml HgTe CQD in hexane would be mixed with 200μL β-ME in DMF, and 5mg TBABr could be added to accelerate the phase transfer process. For typical p-type HgTe CQD, 5mg $(NH_4)_2S$ would be added in CQD/DMF. For typical intrinsic or n-type CQD, 5mg or 20mg $HgCl_2$ salt would be added in this step, respectively. CQDs were precipitated by adding toluene as the anti-solvent, followed by centrifugation. After discarding the supernatant, 40 μL DMF was used to dissolve the CQD solids, yielding a colloidally-stable solution. The CQD films are prepared by spin-coating and followed by solid-phase ligand exchange with ethanedithiol (EDT)/HCl/IPA (1:1:50 by volume) solution for 10 s, rinsed with IPA, and dried with $N_2$. Solid-phase ligand exchange is necessary to remove the extra hybrid ligands, which also fix the Fermi level of the CQD films.

## Photoresponse Characterization

The detector was placed in a cryostat for performance characterization. Responsivity was measured using a calibrated blackbody source at 600°C. The photon flux on the detector was determined by the area of the detector, the area of the blackbody, the distance between the detector and the blackbody, and the spectrum of the blackbody radiation. The photocurrent was amplified first by a preamplifier (Femto DLA-200) and the noise is measured with a spectrum analyzer.

# Imaging

The imaging of CQDs imagers was conducted with a focal plane array tester, which can provide power, ground, timing, and trigger signal. The output channels from the ROICs were sampled and reordered to construct raw images. The performance, both at array and pixels levels, can be assessed. The RMS noise, fixed pattern noise, crosstalk, pixel surface response, and detectivity can be generated. A lens with an F-number of 2 was used. A 30W tungsten lamp was used to introduce SWIR light.

# Declarations

### Acknowledgements

This work was supported by National Key R&D Program of China and National Natural Science Foundation of China (2021YFA0717600, NSFC No. 62035004 and NSFC No.62105022).

### Author contributions

X.T. and M.C. designed and conceived the experiments. S.Z. and C.B. fabricated and characterized the array-format imagers. T.Q. fabricated and characterized the single-pixel trapping-mode photodetectors. Y.H. and J.S. conducted the package of CQDs imagers. Y.L. performed data analysis. All authors contributed to discussions of the manuscript.

### Conflict of interest

The authors declare no competing interests.

### Materials & Correspondence

Correspondence and requests for materials should be addressed to X.T.

# References

1. Nakadai, M., Asano, T. & Noda, S. Electrically controlled on-demand photon transfer between high-Q photonic crystal nanocavities on a silicon chip. Nat. Photonics **16**, 113–118 (2022).
2. Arakawa, Y., Nakamura, T., Urino, Y. & Fujita, T. Silicon photonics for next generation system integration platform. IEEE Commun. Mag. **51**, 72–77 (2013).
3. Liu, W. *et al.* A fully reconfigurable photonic integrated signal processor. Nat. Photonics 2016 *103* **10**, 190–195 (2016).
4. Zhou, T. *et al.* Large-scale neuromorphic optoelectronic computing with a reconfigurable diffractive processing unit. Nat. Photonics 2021 *155* **15**, 367–373 (2021).
5. Piggott, A. Y. *et al.* Inverse design and demonstration of a compact and broadband on-chip wavelength demultiplexer. Nat. Photonics 2015 *96* **9**, 374–377 (2015).

6. Shastri, B. J. *et al.* Photonics for artificial intelligence and neuromorphic computing. Nat. Photonics 2021 152 **15**, 102–114 (2021).
7. Muraviev, A. V., Smolski, V. O., Loparo, Z. E. & Vodopyanov, K. L. Massively parallel sensing of trace molecules and their isotopologues with broadband subharmonic mid-infrared frequency combs. Nat. Photonics 2018 *124* **12**, 209–214 (2018).
8. Jiang, Y., Karpf, S. & Jalali, B. Time-stretch LiDAR as a spectrally scanned time-of-flight ranging camera. Nat. Photonics 2019 *141* **14**, 14–18 (2019).
9. Liu, J., Dai, J., Chin, S. L. & Zhang, X. C. Broadband terahertz wave remote sensing using coherent manipulation of fluorescence from asymmetrically ionized gases. Nat. Photonics 2010 49 **4**, 627–631 (2010).
10. Rogalski, A., Antoszewski, J. & Faraone, L. Third-generation infrared photodetector arrays. J. Appl. Phys. **105**, 091101 (2009).
11. Sood, A. K. *et al.* Development of low dark current SiGe-detector arrays for visible-NIR imaging sensor. https://doi.org/10.1117/12.*852682* **7660**, 204–210 (2010).
12. Tanbakuchi, A. & Soehnel, G. Simulation and experimental characterization of the point spread function, pixel saturation, and blooming of a mercury cadmium telluride focal plane array. *Appl. Opt. Vol. 51, Issue 33, pp. 7987–7993* **51**, 7987–7993 (2012).
13. Deumel, S. *et al.* High-sensitivity high-resolution X-ray imaging with soft-sintered metal halide perovskites. *Nat. Electron.* 2021 *49* **4**, 681–688 (2021).
14. Kim, Y. C. *et al.* Printable organometallic perovskite enables large-area, low-dose X-ray imaging. Nat. 2017 5507674 **550**, 87–91 (2017).
15. Wei, W. *et al.* Monolithic integration of hybrid perovskite single crystals with heterogenous substrate for highly sensitive X-ray imaging. Nat. Photonics *2017 115* **11**, 315–321 (2017).
16. Baierl, D. *et al.* A hybrid CMOS-imager with a solution-processable polymer as photoactive layer. *Nat. Commun.* 2012 *31* **3**, 1–8 (2012).
17. Christopher Buurma, al *et al.* MWIR imaging with low cost colloidal quantum dot films. https://doi.org/10.1117/12.*2239986* **9933**, 993303 (2016).
18. Ciani, A. J., Pimpinella, R. E., Grein, C. H. & Guyot-Sionnest, P. Colloidal quantum dots for low-cost MWIR imaging. https://doi.*org*/10.1117/12.*2234734* **9819**, 333–341 (2016).
19. Kim, J. H. *et al.* Detailed Characterization of Short-Wave Infrared Colloidal Quantum Dot Image Sensors. IEEE Trans. Electron Devices 1–7 (2022). doi:10.1109/TED.2022.3164997
20. Rauch, T. *et al.* Near-infrared imaging with quantum-dot-sensitized organic photodiodes. Nat. Photonics **3**, 332–336 (2009).
21. Goossens, S. *et al.* Broadband image sensor array based on graphene–CMOS integration. Nat. Photonics *2017 116* **11**, 366–371 (2017).
22. Liu, J. *et al.* A near-infrared colloidal quantum dot imager with monolithically integrated readout circuitry. *Nat. Electron.* 2022 *57* **5**, 443–451 (2022).

23. Lan, X. *et al.* Quantum dot solids showing state-resolved band-like transport. *Nat. Mater.* 2020 *193* **19**, 323–329 (2020).
24. Keuleyan, S., Lhuillier, E., Brajuskovic, V. & Guyot-Sionnest, P. Mid-infrared HgTe colloidal quantum dot photodetectors. Nat. Photonics **5**, 489–493 (2011).
25. Konstantatos, G. *et al.* Hybrid graphene–quantum dot phototransistors with ultrahigh gain. Nat. Nanotechnol. **7**, 363–368 (2012).
26. Sun, Z. *et al.* Infrared Photodetectors Based on CVD-Grown Graphene and PbS Quantum Dots with Ultrahigh Responsivity. Adv. Mater. **24**, 5878–5883 (2012).
27. Huo, N., Gupta, S. & Konstantatos, G. $MoS_2$ -HgTe Quantum Dot Hybrid Photodetectors beyond 2 μm. Adv. Mater. **29**, 1606576 (2017).
28. Chen, M. *et al.* High Carrier Mobility in HgTe Quantum Dot Solids Improves Mid-IR Photodetectors. ACS Photonics **6**, 2358–2365 (2019).
29. Chen, M. & Guyot-Sionnest, P. Reversible Electrochemistry of Mercury Chalcogenide Colloidal Quantum Dot Films. ACS Nano **11**, 4165–4173 (2017).
30. Pejovic, V. *et al.* Thin-Film Photodetector Optimization for High-Performance Short-Wavelength Infrared Imaging. IEEE Electron Device Lett. **42**, 1196–1199 (2021).
31. Steckel, J. S. *et al.* 1.62 μglobal Shutter Quantum Dot Image Sensor Optimized for Near and Shortwave Infrared. *Tech. Dig. - Int. Electron Devices Meet. IEDM* **2021-December**, 23.4.1–23.4.4 (2021).
32. Gréboval, C. *et al.* Photoconductive focal plane array based on HgTe quantum dots for fast and cost-effective short-wave infrared imaging. Nanoscale **14**, 9359–9368 (2022).
33. Chen, M. *et al.* Photocurrent Enhancement of HgTe Quantum Dot Photodiodes by Plasmonic Gold Nanorod Structures. ACS Nano **8**, 8208–8216 (2014).
34. Chen, M. *et al.* Fast, Air-Stable Infrared Photodetectors based on Spray-Deposited Aqueous HgTe Quantum Dots. Adv. Funct. Mater. **24**, 53–59 (2014).
35. Jagtap, A. *et al.* Short Wave Infrared Devices Based on HgTe Nanocrystals with Air Stable Performances. J. Phys. Chem. C **122**, 14979–14985 (2018).
36. Yuan, S., Naveh, D., Watanabe, K., Taniguchi, T. & Xia, F. A wavelength-scale black phosphorus spectrometer. Nat. Photonics 2021 158 **15**, 601–607 (2021).
37. Micro- *and Opto-Electronic Materials and Structures: Physics, Mechanics, Design, Reliability, Packaging*. *Micro- and Opto-Electronic Materials and Structures: Physics, Mechanics, Design, Reliability, Packaging* (Springer US, 2007). doi:10.1007/0-387-32989-7
38. JEP122F, J. S. *Failure mechanisms and models for semiconductor devices*. *JEDEC Solid State Technology Association, Arlington, VA* (2010).
39. Tang, X., Chen, M., Ackerman, M. M., Melnychuk, C. & Guyot-Sionnest, P. Direct Imprinting of Quasi-3D Nanophotonic Structures into Colloidal Quantum-Dot Devices. Adv. Mater. **32**, 1906590 (2020).

# Figures

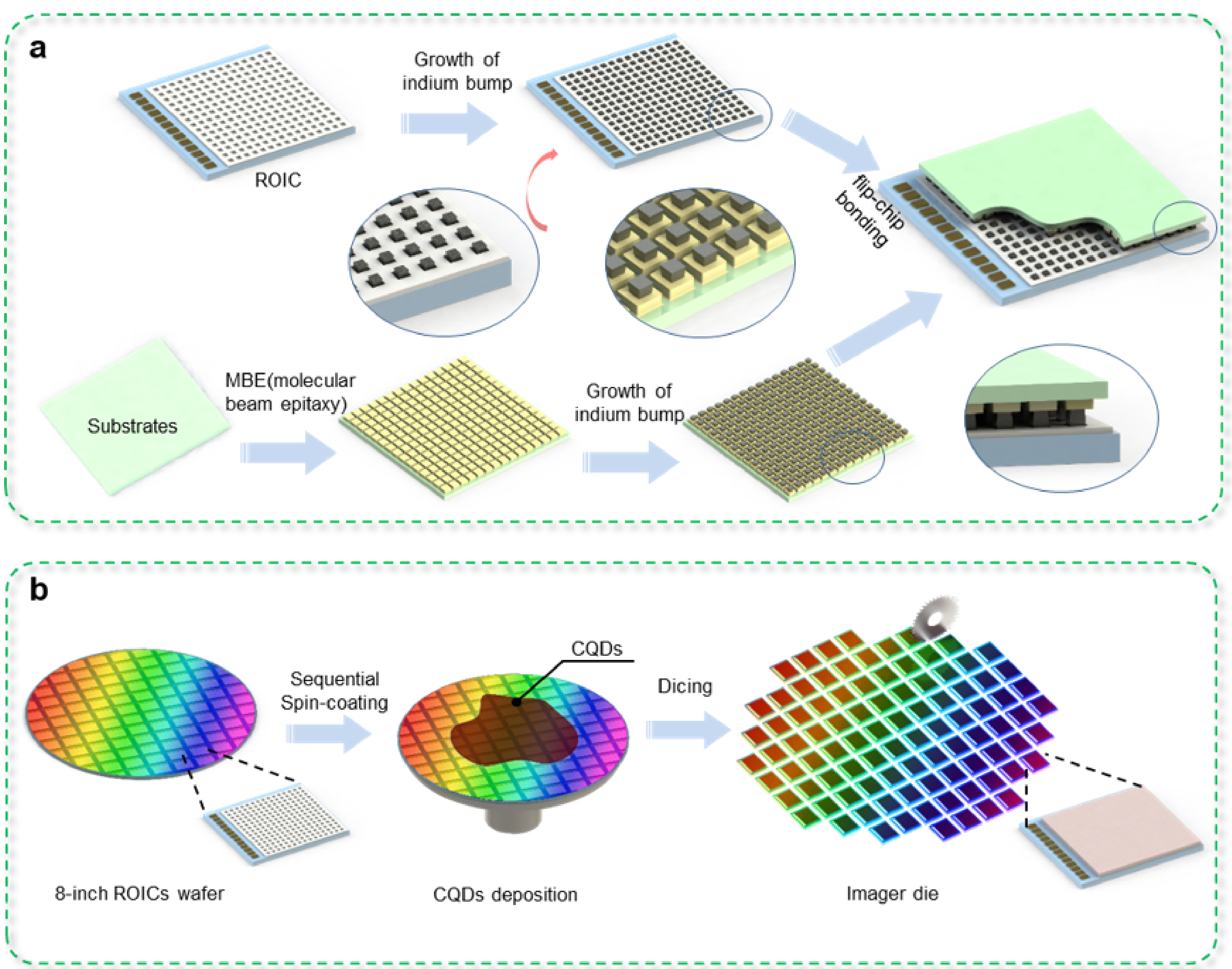


### Figure 1

**Fabrication process of typical infrared imagers. a.** Flip-bonding-based fabrication process of infrared imagers. The process starts with the preparation of lattice-matched substrates. Molecular beam epitaxy was used to grow sensing materials followed by pixelation. Indium bumps pillars were added to both the sensing materials and ROICs. Electrical connections were completed by mechanically pressing the sensing materials onto the ROICs. **b.**CMOS-compatible fabrication of CQDs with Si-ROICs. An 8-inch ROICs wafer was cleaned, followed by the spinning-coating of CQDs solutions. After the thickness of CQDs reaches the desired value. The 8-inch wafer was diced into individual imager chips.

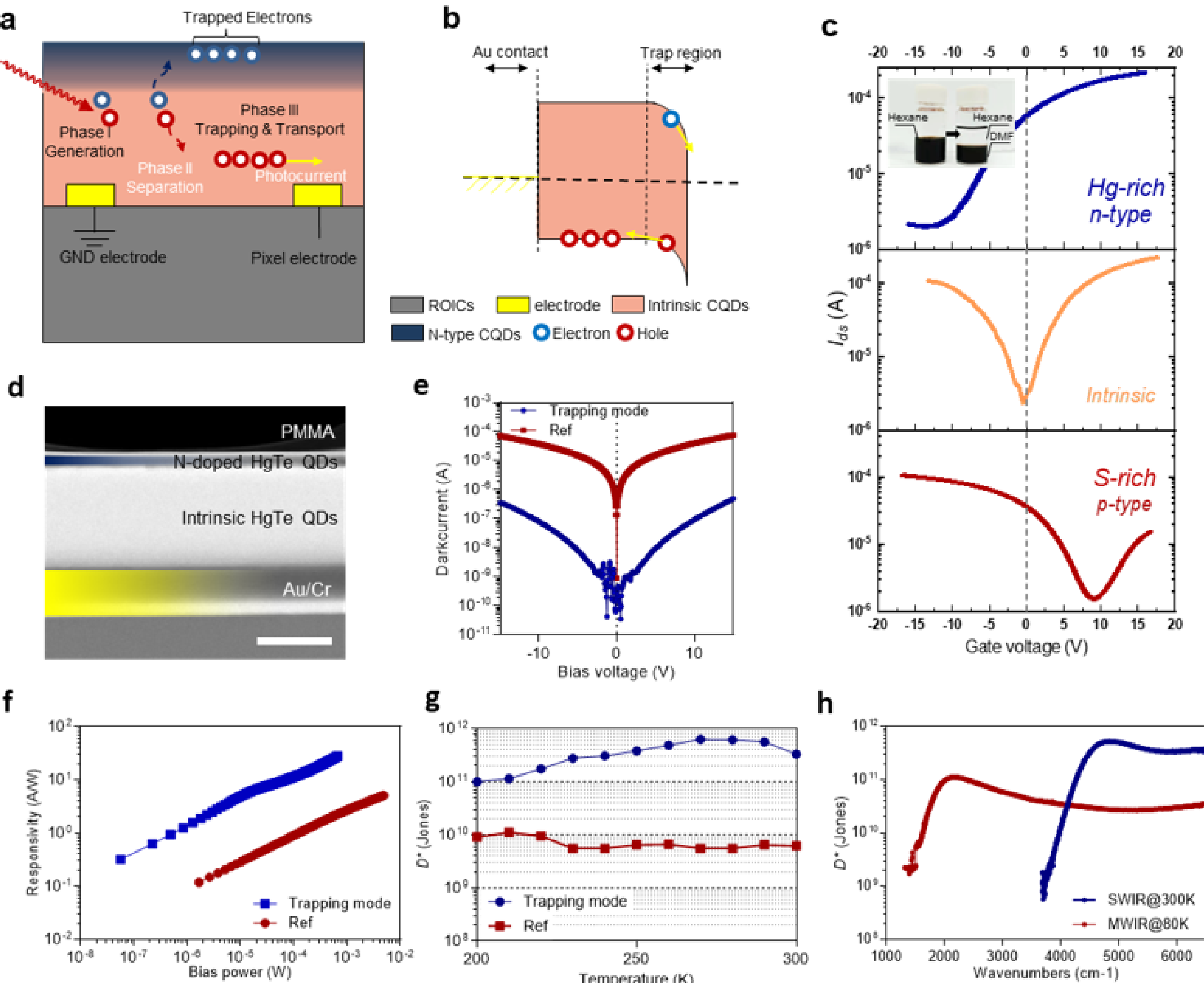


## Figure 2

**Trapping-mode photodetectors**. **a**. Illustration of the working process of trapping-mode photodetectors. **b**. Energy band diagrams of the trapping-mode photodetectors. **c**. Measured field-effect transistor transfer curves of n-doped, intrinsic, and p-doped HgTe CQDs. **d**. Cross-sectional transmission electron microscopy image of the trapping-mode photodetector. The scale bar is 200 nm. **e**. Darkcurrent of a trapping-mode photodetector and reference detector without trapping layer. **f**. Responsivity as a function of bias power for both trapping-mode photodetectors and reference detectors. **g**. Detectivity as a function of operating temperature. **h.**Spectral detectivity curves of trapping-mode photodetectors in SWIR and MWIR ranges.

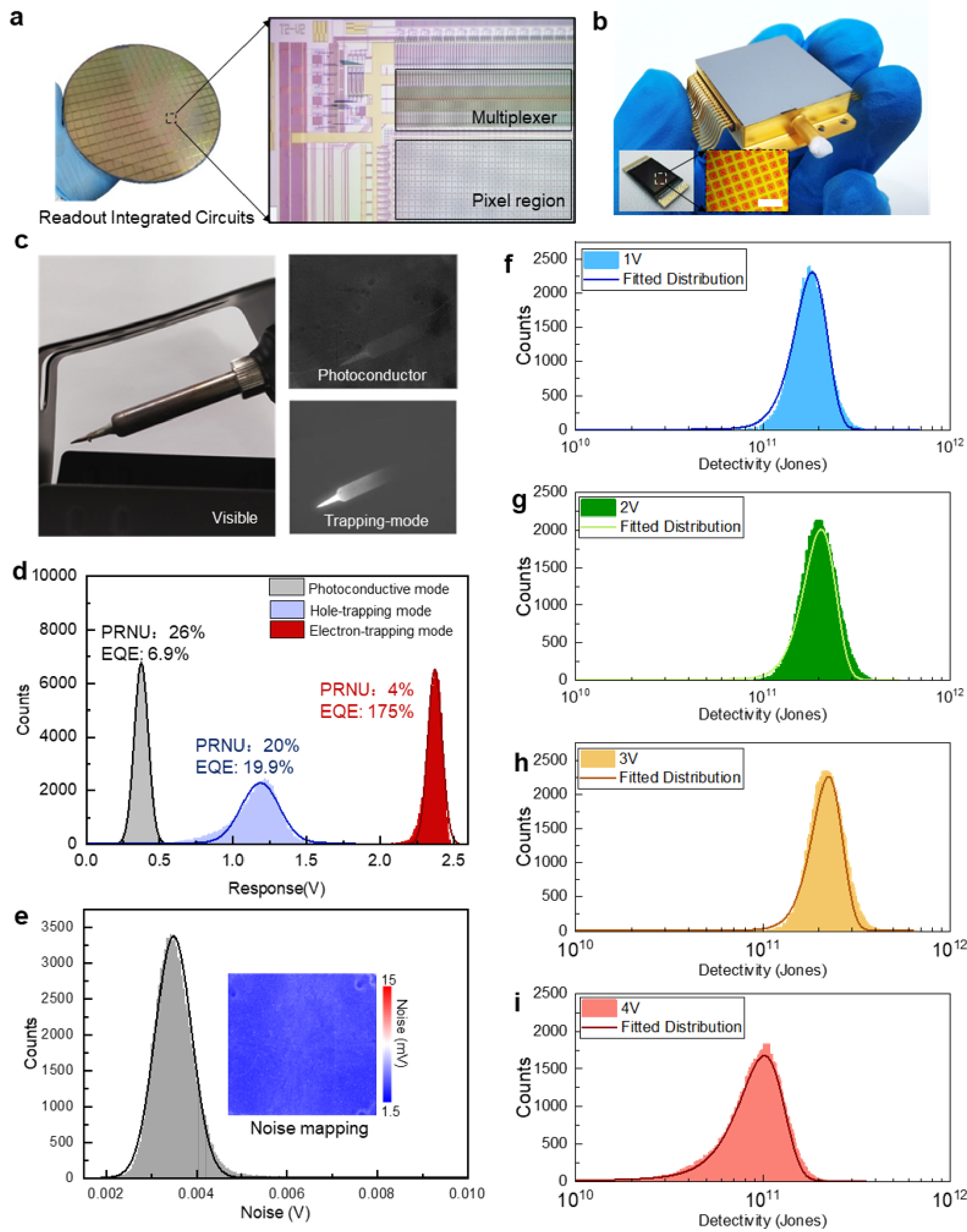


## Figure 3

**Trapping-mode HgTe CQDs imagers. a.** 8-inch ROICs wafer and zoomed view of the pixel region. **b.** Packaged HgTe CQDs imagers with silicon optical window. The inset shows the ROICs deposited with HgTe CQDs and an optical microscopy images of the CQDs pixels. The scale bar is 60μm. **c.** Visible and SWIR images of a soldering iron were captured by (**i**) Si-CMOS imager, (**ii**) $Ag_2Te$ doped photovoltaic imager, (**iii**) photoconductor imager, and (**iv**) trapping-mode imager. The temperature of the tip is 480°C. **d.**

Distribution of the response from each pixel from the photoconductive imager, hole trapping-mode imager, and electron trapping-mode imager. **e.** Distribution of pixels' noise. The inset shows the noise mapping of a trapping-mode imager. Detectivity under bias voltage of (**f**) 1V, (**g**) 2V, (**h**) 3V, and (**i**) 4V. Details of the response and noise can be found in **Table. S4**. Devie performance of 10 representative CQDs imagers is summarized in **Table.S5**.

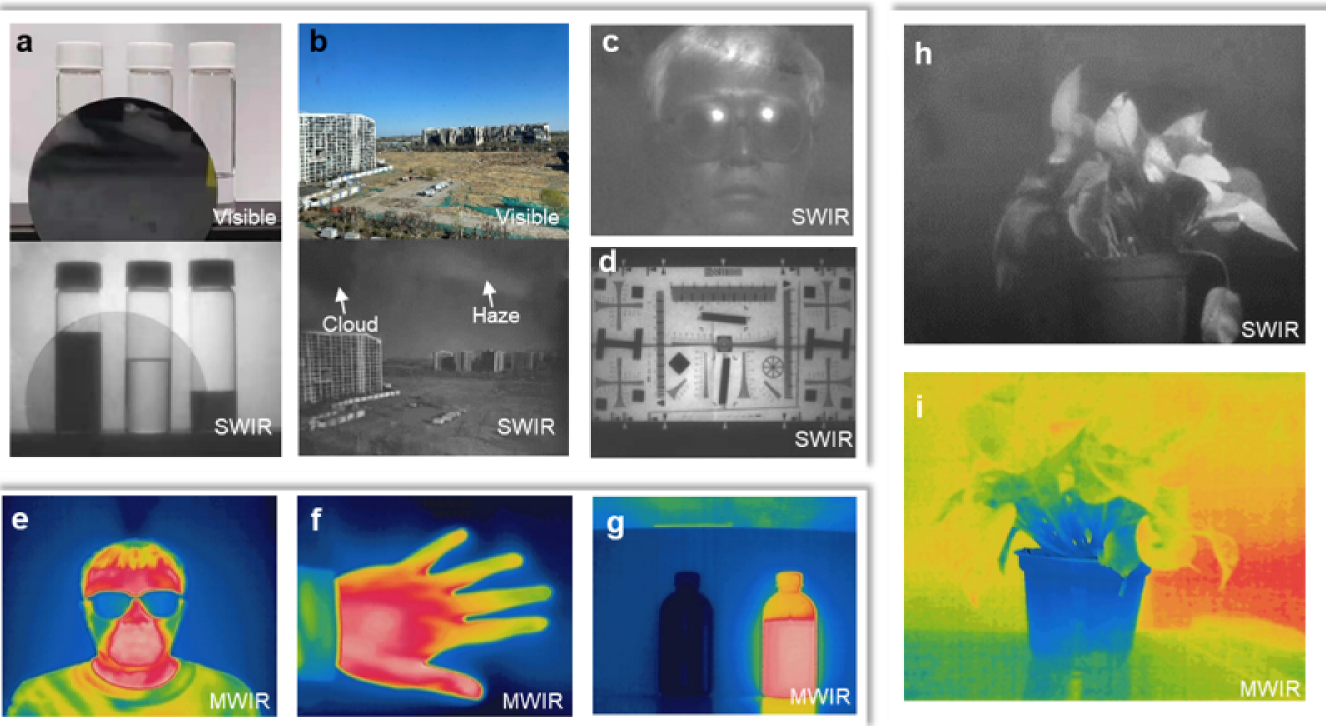


## Figure 4

**Captured infrared images with CQDs imagers. a.** Visible and SWIR images of three bottles of water, tetrachloroethylene, and isopropanol behind a silicon wafer. **b.** Visible and SWIR images of sky and buildings. **c.** SWIR images of a human face with glasses. **d.** SWIR image of ISO-12233 test chart. Thermal images of (**e**) human face, (**f**) human hand, and (**g**) two bottles of cold and hot water.